IEEE Access
Multidisciplinary ⋮ Rapid Review ⋮ Open Access Journal

Received 21 June 2024, accepted 20 July 2024, date of publication 1 August 2024, date of current version 12 August 2024.

Digital Object Identifier 10.1109/ACCESS.2024.3436565

RESEARCH ARTICLE

Unsteady MHD Flow of Casson Hybrid Nanofluid Over an Infinite Vertical Flat Plate: Crank-Nicholson Scheme and Statistical Approach

KEERTHIGA M AND P. BALA ANKI REDDY
Department of Mathematics, School of Advanced Sciences, Vellore Institute of Technology, Vellore 632014, India
Corresponding author: P. Bala Anki Reddy (sireesha.siri7@gmail.com)

ABSTRACT This study investigates the unsteady magnetohydrodynamic flow of Casson hybrid nanofluid over an infinite vertical flat plate under the influence of magnetic flux, heat source/sink, viscous dissipation, and thermal radiation. The considered hybrid nanofluid is the combination of water (70%) and ethylene glycol (30%), together with two dissimilar nanoparticles like magnesium oxide (MgO) and copper oxide (CuO). Initially, the model is formulated as non-linear partial differential equations (PDEs) with independent variables. These equations are converted into a set of dimensionless PDEs using suitable similarity transformations. To acquire the numerical solution, the finite difference (Crank-Nicolson) scheme is employed. The perturbation approach is employed for the analytical solution of the non-dimensional equations. An analysis is conducted to compare numerical and analytical results. As a result, comparisons between analytical and numerical results are more accurate. The study graphically examined the influence of several parameters on velocity and temperature profiles. Additionally, the effects of physical quantities like skin friction coefficient and the Nusselt number have been explained in a table manner. It has been observed from the result, that the velocity profile increases with the Grashof number and permeability parameter, while the magnetic parameter has the opposite effect. Moreover, a multiple regression analysis is also performed to examine the statistical effects of these parameters on the physical quantities. This study has vital applications in several industrial and engineering processes such as the automobile sector, nuclear reactors, solar power systems, HVAC systems, and electronics cooling.

INDEX TERMS Casson fluid, finite difference method, hybrid nanofluid, magnetic field, thermal radiation, viscous dissipation.

I. INTRODUCTION

Non-Newtonian liquids contain a non-linear model, it demonstrates the non-linear interaction between shear stress and the rate of shear. Because of this nonlinearity, various numerical methods have been used to solve such problems. Many liquid polymers and salt explanations appear to be non-Newtonian fluids such as custard, flour, ketchup, toothpaste, shampoo, and blood [1]. Hauswirth et al. [2] explored the non-Newtonian fluid flow of porous media through cross-modelling. Ali et al. [3] examined the peristaltic flows by a non-Newtonian fluid in a curved channel. The Casson fluid flow model is one of the most famous non-Newtonian fluids. It was created by Casson in the year 1959. It has several applications in the pharmaceutical and medical sectors such as proteins, aqueous base plasma, red blood cells, white blood cells, fibrinogen, and haemoglobin. Muhammad Saqib et al. [4] explored the slip effect on the boundary layer of a vertical plate at the beginning of the flows of a Casson fluid. They considered the combined influence of thermal

The associate editor coordinating the review of this manuscript and approving it for publication was Chaitanya U. Kshirsagar.

radiation transfer and mass transfer in the presence of a first-order chemical process. Bala Anki Reddy [5] conducted an investigation into magnetohydrodynamic (MHD) flow through a more rapidly sloped permeability stretched surface. The flow is characterized by the presence of a Casson fluid, heat transmission and chemical processes. Das et al. [6] investigated the effects of the boundary slip along with absorption on solute dispersion in a pulsatile Casson fluid channel flow under a field of magnets. Bhattacharyya et al. [7] studied the exact method for Casson fluid flows through a permeable shrinking plate with changeable wall temperature and heat radiation in the thermal boundary layers.

Nanofluids are colloidal solutions consisting of nanoparticles (usually 1 to 100 nm in size) and a base fluid. Choi [8] were the first to present their concept of nanofluids in order to improve heat transfer with greater conductivities. The function of the nanofluid will determine the choice of base fluid/particle combination. Among the nanoparticles contains metals (*Cu, K, Ag, Al, Si, Ni*), metal oxides (*CuO, ZnO,* TiO_2, Al_2O_3, *MgO,* Fe_2O_3), carbon materials, metal carbides, and metal nitrides. Later on, the nanoparticle was combined with a base fluid, such as water, transformer oil, naphthenic mineral oil, paraffin oil, ethylene glycol, or vegetable oil, to create a nanofluid [9]. Gupta et al. [10] investigated that nanoparticles are classified into numerous types that depend on their size, shape, physical properties, and chemical properties. Tiwari and Das [11] presented two distinct models for analyzing nanofluid characteristics and behavior. Tayyab et al. [12] investigated Darcy-Forchheimer flow, biological convection, and activation energy in a 3-D rotating nanofluid flow using numerical methods. Subba et al. [13] investigated the flow of a mixed convection boundary layer through a vertical wedge in a porous material saturated with nanofluid. In recent years, researchers and scientists have developed a new type of nanofluid that suspends two distinct kinds of nanoparticles in a pure fluid. This novel type of nanofluid is known as a hybrid nanofluid. Hybrid nanofluids can be used in a wide variety of fields such as generator cooling, nuclear reactor coolant, automobile cooling, electro-mechanical, and energy from renewable sources industries. Yasir et al. [14] explored hybrid nanofluid over a rotational flow affected by mass transpiration due to sheet contraction. [15] This article provides a concise review of current developments involving hybrid nanofluids and tiny liquids that are used in several different machining operations such as grinding, turning, and drilling. Akkurt et al. [16] studied the forced convection through turbulence movement of the hybrid combination in an L-shaped channel in three dimensions. Shaik et al. [17] investigated the natural convection within a sinusoidal wavy channel containing a hybrid nanofluid over the effects of a sloped magnetic field along with heat radiation. Rajesh et al. [18] explored analytical approaches to the unstable flow of a hybrid nanofluid with heat transfer through an infinitely vertical sheet with a ramping temperature.

Magnetohydrodynamics (MHD) explains the movement of a fluid that conducts electricity in the existence of a field of magnetic attraction. This phenomenon is also referred to as magneto-fluid dynamics. Magneto-fluids may appear in a variety of forms including saltwater, electrolytes, plasmas, and metallic fluids. In recent times, several scholars in the branch of fluid motion have investigated MHD. In the year 1970, Hannes Alfven received the Nobel Prize in Physics for his remarkable contributions to the field of MHD. Magnetohydrodynamics is used in many kinds of applications such as power plants, flow meters, nuclear reactors, thermal exchange structures, electrostatic filtration systems, and metal purification in its molten state. Ahmed et al. [19] investigated by the MHD transfer of heat and mass-mixed convection flows of Powell-Eyring nanofluid over an effect of thermal radiation. Mahabaleshwar et al. [20] examined the flow of an MHD viscous fluid and heat transmission characteristics, considering the influence of heat radiation and evaporation effects on a stretching sheet. Reddy and Reddy [21] studied a numerical investigation on the unsteady three-dimensional magnetohydrodynamic micropolar movement of fluid across a slandering sheet in a nanofluid flow. Reddy and Goud [22] examined the impact of a magnetic field on the turbulent flow of a tiny water-based fluid subject to MHD, as it passes through an endless flat surface with an inclined temperature gradient, transferring heat through a porous medium. Casson and Williamson's demonstration of the hybrid nanofluid and the use of the MHD boundary surface effects over a stretching cylindrical was explored by Vijatha and Reddy [23]. Bala Anki Reddy et al. [24] investigated the entropy generation in the magnetohydrodynamic stagnation region flow of the cross-nanofluid using artificial neural networks with numerous layers. Ganie et al. [25] examined the stability evaluation of the magnetohydrodynamics (MHD) casson nanofluid combining brownian motion and thermophoretic diffusion. Their research focuses on an expanding or shrinking sheet within a porous medium. Chabani and Mebarek-oudina [26] examined the magnetohydrodynamic (MHD) flow of a hybrid nanofluid in a triangular enclosure containing zigzags and elliptical obstacles. Chamkha [27] conducted a study on the MHD 3-D free convection over a vertically stretched surface incorporating heat generation or absorption.

Thermal radiation is the emission of electromagnetic waves by a substance because of its temperature, with the characteristics of this radiation depending upon the substance's temperature. It is highly significant in engineering and physics, particularly in space exploration and high-temperature operations. Among these applications are nuclear power plants, the polymer processing sector, gas turbines, and different propulsion engines for aircraft, vehicles, missiles, and satellites. Khan and Hamid [28] examined the non-Newtonian thermal radiation's effect on the 2-dimensional unsteady flow that occurs in a Williamson fluid that contains a heat generation /absorption. Reddy and Reddy [29] investigated the influence of mass and heat transfer features of the unsteady hydromagnetic flow through the boundary layer of the viscous fluid across an exponentially

sloped preamble stretched sheet. Alkuhayli [30] explored the heat transfer characteristics of a hybrid nanofluid in motion on a spinning disc while taking into account the effect of thermal radiation. Kumar et al. [31] analyzed the impact of thermal radiation on the magnetohydrodynam-ics transmission of heat caused by the natural convection flow of nanofluids across a vertical plate. Jaafar et al. [32] reviewed the steady movement and transfer of heat of a non-linearly stretching hybrid nanofluid with the effects of MHD, thermal radiation, and the suction function. Jalili et al. [33] examined the non-linear radiative transfer of heat in the occurrence of a magnetic field for non-Newtonian Casson fluids moving over porous media. Goud et al. [34] explored the influence of thermal radiation on the magnetohydrodynamic (MHD) heat transfers on a vertically moving porosity sheet using a micropolar liquid flow. Reddy et al. [35] used a finite element simulation to examine the impact of Soret-Dufour and conjugate heating on the Casson fluid's flow that absorbs heat from a semi-infinite vertical porous plate.

To the author's knowledge, no empirical investigation has been conducted on this topic. Here, the base fluid consists of a mixture of ethylene glycol (30%) and water (70%) while *CuO* and *MgO* are the nanoparticles present in the hybrid nanofluid. The flow considered under consideration are viscous dissipation and the permeability parameter. The non-linear differential systems can be transformed into dimensionless systems with the use of appropriate variables. The finite difference approach results in the execution of numerical computations. An analysis is conducted to compare numerical and analytical results. The graphical analysis is focused on the performance of influential parameters such as velocity and temperature. The specific novelty of this study lies in its examination of the unsteady MHD flow of Casson hybrid nanofluid over an infinite vertical flat plate. Unlike previous studies, such as [36] and [37], which employed the Laplace transforms for analytical solutions. This research utilises the Crank-Nicholson (finite difference method) numerical scheme, providing more accurate and stable solutions. Additionally, we used the statistical approach to validate the results, further enhancing the purpose of this study. This innovative combination of methodologies offers new insights into flow dynamics and heat transfer characteristics, representing a significant advancement over existing research. The findings of this study can be applied in various domains including heating systems, refrigeration processes, heat exchangers, heat pipes, air conditioning systems, and coolant applications in machinery and manufacturing processes.

II. FORMULATING MATHEMATICAL MODEL

Let us consider the unsteady magnetohydrodynamics (MHD) flow of Casson fluid in a porous substance through an infinite vertical flat plate. Assume that the x-axis is parallel to the sheet and the y-axis is perpendicular to the plate. Only fluid

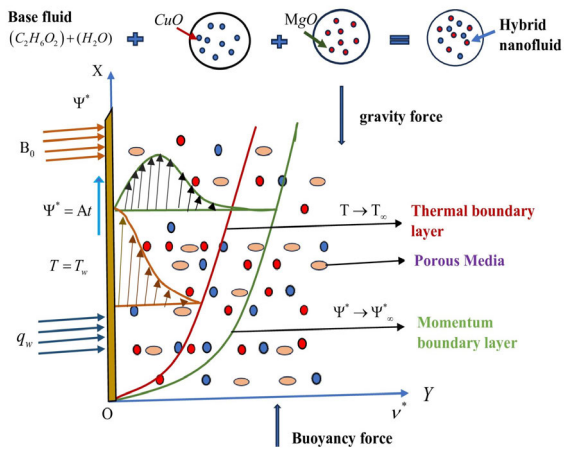

FIGURE 1. Sketch of physical flow problem.

near the plates is taken in at the start of motion $t = 0^+$. The fluid flow experiences an increase when time (t) is greater than zero, as a result of the applied velocity $\Psi^* = At$ and the presence of viscous forces. Currently, a magnetic field with force B_0 being produced to induce fluid flowing in a normal direction. At the same time, the ambient temperature T_∞, at the surface of the plate is being raised T_w. Fig.1 depicts the study model of the subject with coordinates.

The following equation is the isotropic rheological equation that is used for the situation of incompressible flow in a Casson fluid:

$$\pi_{ij} = \begin{cases} 2\left(\dfrac{P_y}{\sqrt{2\pi}} + \mu_B\right) e_{ij} \; ; \pi_c < \pi \\ 2\left(\dfrac{P_y}{\sqrt{2\pi_c}} + \mu_B\right) e_{ij} \; ; \pi_c > \pi \end{cases} \tag{1}$$

where P_y represents the stress generated in a non-Newtonian fluid

$\pi = e_{ij}e_{ij}$, where e_{ij} represents $(i, j)^{th}$ components of a deformation rate

π_c represents the critical value of the product that follows the Casson model.

μ_B represents dynamic viscosity.

The heat flux (q_r) can be defined as a Rosseland approximation:

$$q_r = \frac{-4\sigma_e}{3\beta_r}\frac{\partial T^4}{\partial y} \tag{2}$$

where σ_e is a Stefan-Boltzmann constant and β_r is the absorption coefficient.

Furthermore, temperature difference with the flow T^4 can be obtained in the Taylor series $T^4 \approx (4T - 3T_\infty)\, T_\infty^3$ is obtained by expanding T^4. By excluding higher-order variables, the temperature is determined relative to the ambient temperature. In addition, the present analysis considers the influence of permeability parameters and viscous dissipation.

TABLE 1. Thermo-physical properties of hybrid nanofluid are as follows [23].

Property	Nanoparticles and base fluid
Dynamic viscosity (μ)	$\mathrm{I}_1 = \frac{\mu_{hnf}}{\mu_f} = \frac{1}{(1-\phi_1)^{2.5}(1-\phi_2)^{2.5}}$
Density (ρ)	$\mathrm{I}_2 = \frac{\rho_{hnf}}{\rho_f} = (1-\phi_2)\left[(1-\phi_1)+\phi_1\frac{\rho_{s1}}{\rho_f}\right]+\phi_2\frac{\rho_{s2}}{\rho_f}$
Electrical conductivity (σ)	$\mathrm{I}_3 = \frac{\sigma_{hnf}}{\sigma_{bf}}\times\frac{\sigma_{bf}}{\sigma_f} == \left[\frac{\sigma_{s2}+2\sigma_{bf}-2\phi_2(\sigma_{bf}-\sigma_{s2})}{\sigma_{s2}+2\sigma_{bf}+\phi_2(\sigma_{bf}-\sigma_{s2})}\right]\times\left[\frac{\sigma_{s1}+2\sigma_f-2\phi_1(\sigma_f-\sigma_{s1})}{\sigma_{s1}+2\sigma_f+\phi_1(\sigma_f-\sigma_{s1})}\right]$
Heat capacity (ρc_p)	$\mathrm{I}_4 = \frac{(\rho c_p)_{hnf}}{(\rho c_p)_f} = (1-\phi_2)\left[(1-\phi_1)+\phi_1\frac{(\rho c_p)_{s1}}{(\rho c_p)_f}\right]+\phi_2\frac{(\rho c_p)_{s2}}{(\rho c_p)_f}$
Thermal conductivity (κ)	$\mathrm{I}_5 = \frac{\kappa_{hnf}}{\kappa_{bf}}\times\frac{\kappa_{bf}}{\kappa_f} = \frac{\kappa_{s2}+2\kappa_{bf}-2\phi_2(\kappa_{bf}-\kappa_{s2})}{\kappa_{s2}+2\kappa_{bf}+\phi_2(\kappa_{bf}-\kappa_{s2})}\times\frac{\kappa_{s1}+2\kappa_f-2\phi_1(\kappa_f-\kappa_{s1})}{\kappa_{s1}+2\kappa_f+\phi_1(\kappa_f-\kappa_{s1})}$
Thermal expansion coefficient ($\rho\beta_p$)	$\mathrm{I}_6 = \frac{(\rho\beta_p)_{hnf}}{(\rho\beta_p)_f} = (1-\phi_2)\left[(1-\phi_1)+\phi_1\frac{(\rho\beta_p)_{s1}}{(\rho\beta_p)_f}\right]+\phi_2\frac{(\rho\beta_p)_{s2}}{(\rho\beta_p)_f}$

The governing equations that have been modelled are expressed [37] in the following form:

$$\frac{\partial \Psi^*}{\partial x} + \frac{\partial v^*}{\partial y} = 0 \tag{3}$$

$$\rho_{hnf}\frac{\partial \Psi^*}{\partial t} = \mu_{hnf}\left(1+\frac{1}{\beta}\right)\frac{\partial^2 \Psi^*}{\partial y^2} + g\,(\rho\beta_T)_{hnf}(\mathrm{T}-\mathrm{T}_\infty) - \sigma_{hnf}\beta_0^2\Psi^* - \frac{\mu_{hnf}}{k^*}\Psi^* \tag{4}$$

$$(\rho c_p)_{hnf}\frac{\partial T}{\partial t} = \kappa_{hnf}\frac{\partial^2 T}{\partial y^2} + \frac{16\sigma_e T_\infty^3}{3\beta_r}\frac{\partial^2 T}{\partial y^2} + Q_0\,(T-T_\infty) + \mu_{hnf}\left(1+\frac{1}{\beta}\right)\left(\frac{\partial \Psi^*}{\partial y}\right)^2 \tag{5}$$

The following are the boundary terms and conditions:

$$y > 0 : \Psi^*(y,0) = 0,\ T(y,0) = T_\infty;\ t \le 0 \tag{6}$$

$$\left.\begin{array}{l} y = 0 : \Psi^*(0,t) = At,\ T(0,t) = T_w \\ y \to \infty : \Psi^* \to \Psi^*_\infty(t) = 0,\ T \to T_\infty(t) \end{array}\right\} t > 0 \tag{7}$$

III. NON-DIMENSIONAL APPROACH

Considering the dimensionless transformation of the governing model, we establish the following non-dimensional variables along with functions:

$$\Psi = \frac{\Psi^*}{(\vartheta_f A)^{1/3}},\quad x = \frac{yA^{1/3}}{\vartheta_f^{2/3}},\quad \tau = \frac{tA^{2/3}}{\vartheta_f^{1/3}},$$

$$\Theta = \frac{(\mathrm{T}-\mathrm{T}_\infty)}{(\mathrm{T}_w-\mathrm{T}_\infty)},\quad Gr = \frac{g\beta_{Tf}\,(\mathrm{T}_w-\mathrm{T}_\infty)}{A},$$

$$\mathrm{Re}_x = \frac{(\vartheta_f \mathrm{A})^{1/3}x}{\vartheta_f},\quad \mathrm{M} = \frac{\sigma_f B_o^2 \vartheta_f^{1/3}}{\rho_f A^{2/3}},\quad \mathrm{Pr} = \frac{(\mu C_p)_f}{k_f}$$

$$\mathrm{Nr} = \frac{16\sigma_e T_\infty^3}{3\beta_r k_f},\quad Q = \frac{Q_0 \vartheta_f^{1/3}}{(\rho C_p)_f A^{2/3}},\quad \mathrm{K} = \frac{k^*(\vartheta_f A)^{\frac{2}{3}}}{(\vartheta_f)^2},$$

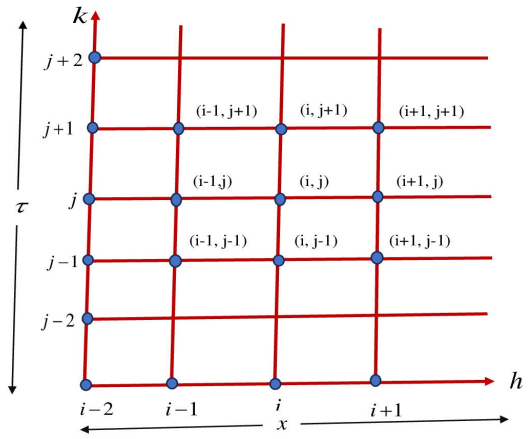

FIGURE 2. Finite difference scheme.

$$Ec = \frac{\left(\vartheta_f A\right)^{2/3}}{\left(c_p\right)_f \left(\mathrm{T}_w - \mathrm{T}_\infty\right)} \tag{8}$$

Using equation (8), the following modifications are made to equations (4) – (5):

$$\mathrm{I}_2 \frac{\partial \Psi}{\partial \tau} = \mathrm{I}_1 \left(1 + \frac{1}{\beta}\right) \frac{\partial^2 \Psi}{\partial x^2} + \mathrm{I}_6 Gr\, \Theta - \mathrm{I}_3 M \Psi - \mathrm{I}_1 \frac{\Psi}{K} \tag{9}$$

$$\mathrm{I}_4 \frac{\partial \Theta}{\partial \tau} = \frac{1}{pr} \left(\mathrm{I}_5 + \mathrm{N}r\right) \frac{\partial^2 \Theta}{\partial x^2} + Q\, \Theta + \mathrm{I}_1 Ec \left(1 + \frac{1}{\beta}\right) \left(\frac{\partial \Psi}{\partial x}\right)^2 \tag{10}$$

Similarly, the boundary conditions have been modified as below.

$$x > 0;\ \Psi(x, 0) = 0,\ \Theta(x, 0) = 0;\ \tau \le 0 \tag{11}$$

$$\left.\begin{array}{l} x = 0;\ \Psi(0, \tau) = \tau,\ \Theta(0, \tau) = 1 \\ x \to \infty;\ \Psi \to \Psi_\infty(\tau) = 0,\ \Theta \to \Theta_\infty(\tau) = 0 \end{array}\right\} \tau > 0 \tag{12}$$

IV. METHOD OF SOLUTION

A. FINITE DIFFERENCE SCHEME

A finite difference method (FDM) is a very effective method for dealing with ordinary differential equations, partial differential problems, and integral equations. This method has been used in different engineering fields, including thermal transport, solid-state mechanics, biofluid factors, geomechanics, and chemical manufacturing. Applying the quasi-linearization method, it is possible to convert the original non-linear flow equations into a linear system. Fig. 2 displayed the Finite difference method. To solve a Partial differential equation (PDE) such as (9)-(10) using FDM, the following four phases are required:

- Domain discretization,
- Analysing the problem through a distinct time period,
- Replacing the derivatives for finite differences,

TABLE 2. Thermodynamics and physical properties are as follows [38].

	EG (30%) + water (70%)	CuO	MgO
$\rho\left(\frac{kg}{m^3}\right)$	1038	6320	3580
$c_\rho\left(\frac{Jkg^{-1}}{\mathrm{K}}\right)$	3714	531.8	960
$K\left(\frac{Wm^{-1}}{k}\right)$	0.484	76.5	48.4
$\sigma\left(\frac{s}{m}\right)$	0.0045	$6.9\text{x}10^{-2}$	$1.42\text{x}10^{-3}$

- Create a recursive technique.

The implicit Crank-Nicolson method is applied to solve the partial differential equations (9)-(10) and the boundary conditions (11) and (12). The Crank-Nicolson method is utilized for substituting the values of velocity and temperature. The resulting terms of this scheme are as follows [39]:

$$\Psi = \Psi_i^j \tag{13}$$

$$\frac{\partial \Psi}{\partial \tau} = \frac{\Psi_i^{j+1} - \Psi_i^j}{\Delta \tau} \tag{14}$$

$$\left(\frac{\partial \Psi}{\partial x}\right) = \frac{\Psi_{i+1}^{j+1} - \Psi_{i-1}^{j+1} + \Psi_{i+1}^j - \Psi_{i-1}^j}{4(\Delta x)} \tag{15}$$

$$\frac{\partial^2 \Psi}{\partial x^2} = \frac{1}{2} \left(\left\{ \frac{\Psi_{i-1}^j - 2\Psi_i^j + \Psi_{i+1}^j}{(\Delta x)^2} \right\} + \left\{ \frac{\Psi_{i-1}^{j+1} - 2\Psi_i^{j+1} + \Psi_{i+1}^{j+1}}{(\Delta x)^2} \right\} \right) \tag{16}$$

While inserting equations (13) to (16) into equation (9) we obtained the discretized version of the governing equation as

$$\frac{\Psi_i^{j+1} - \Psi_i^j}{\Delta \tau} = \frac{\mathrm{I}_1}{\mathrm{I}_2} \left(1 + \frac{1}{\beta}\right) \frac{1}{2} \left(\left\{ \frac{\Psi_{i-1}^j - 2\Psi_i^j + \Psi_{i+1}^j}{(\Delta x)^2} \right\} + \left\{ \frac{\Psi_{i-1}^{j+1} - 2\Psi_i^{j+1} + \Psi_{i+1}^{j+1}}{(\Delta x)^2} \right\} \right) + \frac{\mathrm{I}_6}{\mathrm{I}_2} Gr \Theta_i^j - \frac{\mathrm{I}_3}{\mathrm{I}_2} \mathrm{M} \Psi_i^j - \frac{\mathrm{I}_1}{\mathrm{I}_2} \frac{\Psi_i^j}{K} \tag{17}$$

$$\Psi_i^{j+1} - \Psi_i^j = \frac{\mathrm{I}_1}{\mathrm{I}_2} \left(1 + \frac{1}{\beta}\right) \frac{\Delta \tau}{2\,(\Delta x)^2} \times \left(\begin{array}{l} \Psi_{i-1}^j - 2\Psi_i^j + \Psi_{i+1}^j + \\ \Psi_{i-1}^{j+1} - 2\Psi_i^{j+1} + \Psi_{i+1}^{j+1} \end{array} \right) + \frac{\Delta \tau\ \mathrm{I}_6}{\mathrm{I}_2} Gr \Theta_i^j - \frac{\Delta \tau\, \mathrm{M}\, \mathrm{I}_3}{\mathrm{I}_2} \Psi_i^j - \frac{\Delta \tau\, \mathrm{I}_1}{K\ \ \mathrm{I}_2} \Psi_i^j \tag{18}$$

Let us assume the subsequent quantities for the sake of simplicity,

$$R_1 = \frac{\mathrm{I}_1}{\mathrm{I}_2}\left(1+\frac{1}{\beta}\right)\frac{\Delta\tau}{2\,(\Delta x)^2},\quad S_1 = \frac{\Delta\tau\, Gr\, \mathrm{I}_6}{\mathrm{I}_2},$$
$$T_1 = \frac{\Delta\tau\, \mathrm{M}\, \mathrm{I}_3}{\mathrm{I}_2},\quad U_1 = \frac{\Delta\tau\, \mathrm{I}_1}{K\ \mathrm{I}_2} \tag{19}$$

After incorporating those values into equation (18), we get

$$\Psi_i^{j+1} - \Psi_i^j = R_1\begin{pmatrix}\Psi_{i-1}^j - 2\Psi_i^j + \Psi_{i+1}^j \\ +\Psi_{i-1}^{j+1} - 2\Psi_i^{j+1} + \Psi_{i+1}^{j+1}\end{pmatrix} + S_1\Theta_i^j - T_1\Psi_i^j - U_1\Psi_i^j \tag{20}$$

$$-R_1\Psi_{i-1}^{j+1} + (1+2R_1)\Psi_i^{j+1} - R_1\Psi_{i+1}^{j+1} = R_1\Psi_{i+1}^{j+1} + (1-2R_1-T_1-U_1)\,\Psi_i^{j+1} + R_1\Psi_{i-1}^{j+1} + S_1\Theta_i^j \tag{21}$$

Equation (21) shows implicit finite-difference equations; this is the discrete version of the governing fluid. The outcome of equation (21) can be determined at any given space node as well as time level, denoted as i and τ_{j+1}, respectively. At these specified locations, there are three undetermined coefficients remaining on the right-hand side. These coefficients are situated on the space points *i+1*, *i*, and *i-1* at τ_{j+1}. In a block tridiagonal matrix representation, is AU=B if U is an undetermined column of size (N − 1) and A is a matrix of size (N − 1) × (N − 1) The values of the coefficients that are distributed to the inner nodes can be provided as follows:

$$r_j = -R_1\ ,\quad s_j = (1+2R_1)\ ,$$
$$t_j = (1-2R_1-T_1-U_1)\,\Psi_i^{j+1},$$
$$u_j = R_1\Psi_{i+1}^{j+1}\ ,\ v_j = R_1\Psi_{i-1}^{j+1}\ ,\ w = S_1\Theta_i^j$$
$$for\ i = 2, 3, 4, \ldots\ldots..(N-1)$$

Therefore, equation (21) can be expressed as

$$r_j\Psi_{i-1}^{j+1} + s_j\Psi_i^{j+1} + r_j\Psi_{i+1}^{j+1} = u_j + v_j + t_j + w \tag{22}$$

The given expression describes a system of linear equations in the form of a block tridiagonal matrix.

$$\begin{bmatrix} r_2 & s_2 & 0 & 0 & 0 & 0 & & 0 \\ 0 & r_3 & s_3 & r_3 & . & 0 & & 0 \\ 0 & 0 & . & . & . & . & & 0 \\ 0 & 0 & 0 & . & . & . & & . \\ 0 & 0 & 0 & 0 & r_{\mathrm{N}-1} & s_{\mathrm{N}-1} & & r_{\mathrm{N}-1} \end{bmatrix} \begin{bmatrix} \Psi_1^{j+1} \\ \Psi_2^{j+1} \\ . \\ . \\ \Psi_{\mathrm{N}-1}^{j+1} \end{bmatrix} = \begin{bmatrix} t_2 \\ t_3 \\ . \\ . \\ t_{\mathrm{N}-1} \end{bmatrix}$$
$$+ \begin{bmatrix} u_2 \\ u_3 \\ . \\ . \\ u_{\mathrm{N}-1} \end{bmatrix} + \begin{bmatrix} v_2 \\ v_3 \\ . \\ . \\ v_{\mathrm{N}-1} \end{bmatrix} + \begin{bmatrix} w \\ w \\ . \\ . \\ w \end{bmatrix}$$

Similarly, we solve the equation (9) as follows:

$$\frac{\Theta_i^{j+1} - \Theta_i^j}{\Delta\tau} = \frac{1}{\mathrm{I}_4\mathrm{Pr}}\,(\mathrm{I}_5 + \mathrm{N}r)$$
$$\frac{1}{2}\left(\begin{Bmatrix}\frac{\Theta_{i-1}^j - 2\Theta_i^j + \Theta_{i+1}^j}{(\Delta x)^2}\end{Bmatrix} + \begin{Bmatrix}\frac{\Theta_{i-1}^{j+1} - 2\Theta_i^{j+1} + \Theta_{i+1}^{j+1}}{(\Delta x)^2}\end{Bmatrix}\right) + \frac{Q}{\mathrm{I}_4}\Theta_i^j + \frac{\mathrm{I}_1}{\mathrm{I}_4}Ec\left(1+\frac{1}{\beta}\right) \times\left(\frac{\Psi_{i+1}^{j+1} - \Psi_{i-1}^{j+1} + \Psi_{i+1}^j - \Psi_{i-1}^j}{4(\Delta x)}\right) \tag{23}$$

Multiplying through by $\Delta\tau$,

$$\Theta_i^{j+1} - \Theta_i^j = \frac{1}{\mathrm{I}_4\mathrm{Pr}}\begin{pmatrix}\Theta_{i-1}^j - 2\Theta_i^j + \Theta_{i+1}^j + \\ \Theta_{i-1}^{j+1} - 2\Theta_i^{j+1} + \Theta_{i+1}^{j+1}\end{pmatrix} (\mathrm{I}_5 + \mathrm{N}r)\,\frac{\Delta\tau}{2\,(\Delta x)^2} + \frac{\Delta\tau Q}{\mathrm{I}_4}\Theta_i^j + \frac{\Delta\tau\ \mathrm{I}_1}{\mathrm{I}_4}Ec \left(1+\frac{1}{\beta}\right)\left(\frac{\Psi_{i+1}^{j+1} - \Psi_{i-1}^{j+1} + \Psi_{i+1}^j - \Psi_{i-1}^j}{4(\Delta x)}\right)^2 \tag{24}$$

For simplicity, let us assume the following variables:

$$R_2 = \frac{1}{\mathrm{P}r}\left(\frac{\mathrm{I}_5 + \mathrm{N}r}{\mathrm{I}_4}\right)\frac{\Delta\tau}{2\,(\Delta x)^2},\quad S_2 = \frac{\Delta\tau Q}{\mathrm{I}_4},$$
$$\mathrm{T}_2 = \left(1+\frac{1}{\beta}\right)\frac{\Delta\tau\, Ec\ \mathrm{I}_1}{16(\Delta x)^2\mathrm{I}_4},$$
$$\mathrm{X} = \left(\Psi_{i+1}^{j+1} - \Psi_{i-1}^{j+1} + \Psi_{i+1}^j - \Psi_{i-1}^j\right)^2$$

Applying the above values to equation (24) we get

$$\Theta_i^{j+1} - \Theta_i^j = R_2\begin{pmatrix}\Theta_{i-1}^j - 2\Theta_i^j + \Theta_{i+1}^j + \\ \Theta_{i-1}^{j+1} - 2\Theta_i^{j+1} + \Theta_{i+1}^{j+1}\end{pmatrix} + S_2\Theta_i^j + T_2X \tag{25}$$

$$-R_2\Theta_{i-1}^{j+1} + (1+2R_2)\,\Theta_i^{j+1} - R_2\Theta_{i+1}^{j+1} = R_2\Theta_{i+1}^j + (1-2R_2-S_2)\,\Theta_i^j + R_2\Theta_{i-1}^j + T_2X \tag{26}$$

The finite difference equations (26) derived at a given space node, denoted as i, and at a specific time level denoted as τ_{j+1} consist of three coefficients belonging to space nodes: *i+1*, *i,* and *i-1* preceding at τ_{j+1}. The equations can be represented in matrix form as AU = B, where U indicates an unknown column vector of size (N − 1) at the time level τ_{j+1} then B is a known vector of order (N − 1) that represents the value of U at the n^{th} time level. The coefficient of the square matrix A of order (N − 1) × (N − 1) and a block tridiagonal structure. These expressions will be used to symbolize the coefficients of the interior nodes:

$$d_j = -R_2,\quad e_j = 1+2R_2,\quad f_j = R_2\Theta_{i+1}^j,$$
$$g_j = (1-2R_2-S_2)\,\Theta_i^j,\quad h_j = R_2\Theta_{i-1}^j,$$
$$l = T_2X\quad for\quad i = 2, 3, 4, \ldots\ldots, (\mathrm{N}-1)$$

Hence, equation (26) can be formulated as

$$d_j\Theta_{i-1}^{j+1} + e_j\Theta_i^{j+1} + d_j\Theta_{i+1}^{j+1} = f_j + g_j + h_j + l \tag{27}$$

The equation (27) creates a system of linear equations, that can be expressed in block tridiagonal matrix form as

$$\begin{bmatrix} d_2 & e_2 & 0 & 0 & 0 & 0 & 0 \\ 0 & d_3 & e_3 & d_3 & . & 0 & 0 \\ 0 & 0 & . & . & . & . & 0 \\ 0 & 0 & 0 & . & . & . & . \\ 0 & 0 & 0 & 0 & d_{N-1} & e_{N-1} & d_{N-1} \end{bmatrix} \begin{bmatrix} \Theta_1^{j+1} \\ \Theta_2^{j+1} \\ . \\ . \\ \Theta_{N-1}^{j+1} \end{bmatrix} = \begin{bmatrix} f_2 \\ f_3 \\ . \\ . \\ f_{N-1} \end{bmatrix} + \begin{bmatrix} g_2 \\ g_3 \\ . \\ . \\ g_{N-1} \end{bmatrix} + \begin{bmatrix} h_2 \\ h_3 \\ . \\ . \\ h_{N-1} \end{bmatrix} + \begin{bmatrix} l \\ l \\ . \\ . \\ l \end{bmatrix}$$

B. PERTURBATION ANALYSIS

Equations (9) to (10) represent a non-linear partial differential equation system. These equations do not have a closed-form solution that can be obtained by utilizing the given initial and boundary conditions (12). This can be represented by depicting the velocity and temperature equation of the fluid. Using equation (9) – (10) and equating the harmonic and non-harmonic terms, we are able to arrive at the following result:

$$\begin{aligned} &\mathrm{I}_1\left(1+\frac{1}{\beta}\right)(\Psi_0)_{x,x}+\mathrm{I}_6 Gr\Theta-\mathrm{I}_3\mathrm{M}\Psi_0(x)-\mathrm{I}_1\frac{\Psi_0(x)}{\mathrm{K}}=0 \\ &\frac{\mathrm{I}_1\left(1+\frac{1}{\beta}\right)(\Psi_1)_{x,x}-\mathrm{I}_3\mathrm{M}\Psi_1(x)-\mathrm{I}_1\frac{\Psi_1(x)}{\mathrm{K}}}{e^{\mathrm{I}t}}=0 \end{aligned} \tag{28}$$

$$\begin{aligned} &-\mathrm{I}_4\Theta_\tau+\frac{(\mathrm{I}_5+\mathrm{N}r)\Theta_{x,x}}{\mathrm{P}r}+\mathrm{I}_1\left(1+\frac{1}{\beta}\right)\mathrm{E}c(\Psi_0)_{x,x} \\ &+Q\Theta=0 \\ &\frac{\mathrm{I}_1\left(1+\frac{1}{\beta}\right)\mathrm{E}c(\Psi_1)_{x,x}}{e^{\mathrm{I}t}}=0 \end{aligned} \tag{29}$$

The constraints on the boundary for the expression (12) become:

$$\begin{aligned} &\Psi_0(0)=1,\ \Theta_0(0)=1, \Psi_0(9)=0, \Theta_0(9)=0 \\ &\Psi_1(0)=1,\ \Theta_1(0)=1,\ \Psi_1(9)=0,\ \Theta_1(9)=0 \end{aligned} \tag{30}$$

V. PHYSICAL QUANTITIES

A. NUSSELT NUMBER

The Nusselt number is a non-dimensional quantity that measures the ratio of convective heat transfer to conductive heat transfer. It was originally formulated by Wilhelm Nusselt, a German engineer using mathematical analysis.

In dimensionless form, the Nusselt number is

$$\mathrm{N}u_x=\frac{xq_w}{k_f(\mathrm{T}_w-\mathrm{T}_\infty)} \tag{31}$$

where the heat flux q_w is

$$q_w=-\left(k_{hnf}+\frac{16\sigma^*\mathrm{T}_\infty^3}{3k^*}\right)\left(\frac{\partial \mathrm{T}}{\partial y}\right)\Big|_{y=0}$$

We have

$$\mathrm{N}u_x\mathrm{Re}_x^{-1}=-(\mathrm{I}_5+\mathrm{N}r)\left(\frac{\partial\Theta}{\partial x}\right)_{x=0} \tag{32}$$

B. SKIN FRICTION COEFFICIENT

Skin friction is a form of drag force exerted by a solid plate on a fluid in motion. Skin friction is caused by viscous force in fluids and ranges from laminar to turbulent flows, depending on the fluid's velocity.

In non-dimensional form, the Skin friction coefficient is

$$C_{fx}=\frac{\tau_w}{\rho_f\left(\vartheta_f\mathrm{A}\right)^{\frac{2}{3}}} \tag{33}$$

where, the shear stress τ_w is

$$\tau_w=\mu_{hnf}\left(1+\frac{1}{\beta}\right)\frac{\partial\Psi^*}{\partial y}\Big|_{y=0}$$

We have

$$C_{fx}=\mathrm{I}_1\left(1+\frac{1}{\beta}\right)\left(\frac{\partial\Psi}{\partial x}\right)_{x=0} \tag{34}$$

VI. GRAPHICAL ANALYSIS

The current work examines the impact of MHD Casson hybrid nanofluid flow and heat transfer characteristics of an incompressible fluid. In this research, *CuO* and *MgO* as nanoparticles are used, followed by a base fluid consisting of ethylene glycol and water, resulting in a hybrid nanofluid. Here, the volume fraction of copper oxide (*CuO*) nanoparticles denoted as ϕ_1 and the volume fraction of magnesium oxide *(MgO)* nanoparticles as ϕ_2. This part explains the influences of distinct flow variables on the velocity profile $\Psi(x,\tau)$ and temperature profile $\Theta(x,\tau)$. Table 1 shows the thermal properties of two different nanoparticles and base fluid. Table 2 represents the thermo-physical properties of hybrid nanoparticles. Meanwhile, skin friction and Nusselt numbers are numerically evaluated and represented in Tables 3 and 4. Fig. 3 displays the flowchart of implicit finite difference through the Crank-Nicolson method. The flow is described by the Prandtl number (Pr), the Grashof number (Gr), the thermal radiation parameter (Nr), the permeability parameter (K), heat source/sink parameter (Q), magnetic parameter (M), and Eckert number (Ec). The numerical technique utilized for the entire problem depends on the non-dimensional elements. These are some fixed pertinent parameters are $\mathrm{M}=0.5, \mathrm{K}=1, Gr=5, \mathrm{N}r=1, \mathrm{E}c=0.3Q=0.2, \beta=0.5, \phi_1=0.02$ and $\phi_2=0.02$. The presence of upper or lower arrows in the graphs implies that is either increasing or decreasing.

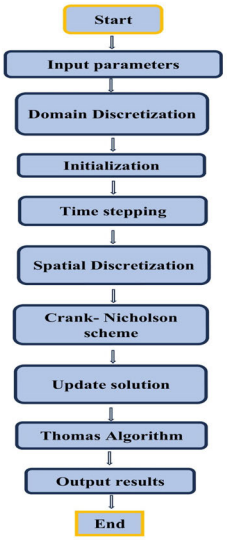

FIGURE 3. Crank nicholson scheme.

A. EFFECT OF M, Gr, K, ϕ_1 AND ϕ_2 ON THE VELOCITY PROFILES $\Psi(x, \tau)$

Figs (4)-(11) are depicted to show the physical behaviour of each parameter that is M, Gr, K, ϕ_1 and ϕ_2 on the velocity profile ($\Psi(x, \tau)$). Figs. 4 and 5 illustrate the impact of magnetic parameter (M) on the velocity profiles $\Psi(x, \tau)$ Fig. 4 illustrates a comparison between Newtonian and non-Newtonian fluids circumstances, whereas Fig. 5 compares scenarios involving nanofluids and hybrid nanofluids, both with the same parameters. Here, it can be seen that as the value of M increases, the velocity profiles decrease in both comparison cases. In physical terms, when a magnetic parameter is applied to an electrically conductive fluid, it generates a Lorentz force. This force tends to slow down the fluid flow by opposing its motion. As the magnetic field strength increases, the Lorentz force becomes more powerful, resulting in a reduced velocity profile for the fluid. Figs. 6 and 7 show the effects of the Grashof number Gr on the velocity patterns ($\Psi(x, \tau)$). Fig. 6 presents a comparison of scenarios involving Newtonian and non-Newtonian fluids. Fig. 7, on the other hand, compares nanofluids and hybrid nanofluids for an infinite vertical flat plate, with the same parameter Gr. In these comparisons, it is observed that the velocity rises as the value increases since the buoyancy exerted on the fluid elements by gravitational forces enhances the velocity of the fluid. Figs. 8 and 9 show the effects of the permeability parameter (K) on velocity profile $\Psi(x, \tau)$. Fig. 8 shows a comparison between Newtonian and non-Newtonian fluids. Fig. 9 shows a comparison between the results of the hybrid nanofluid and the nanofluid. The velocity profile is enhanced to provide a more accurate evaluation of the permeability parameter. The visual representation of the flow is demonstrated. When the fluid flows through a region with greater porosity, it experiences reduced resistance to flow in the opposite direction. As the permeability parameter increases, the fluid encounters a reduced barrier to flow, resulting in an increased velocity profile. Figs. 10 and 11 illustrate how the volume fractions of nanoparticles ϕ_1 (CuO) and ϕ_2 (MgO) affect the velocity fields $\Psi(x, \tau)$ when comparing Newtonian and non-Newtonian scenarios. This scenario results in an increase in the values of ϕ_1 and ϕ_2 which indicates a corresponding increase in the velocity profile.

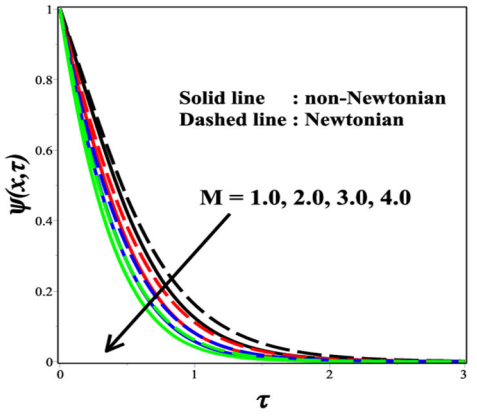

FIGURE 4. Influence of M on $\Psi(x, \tau)$.

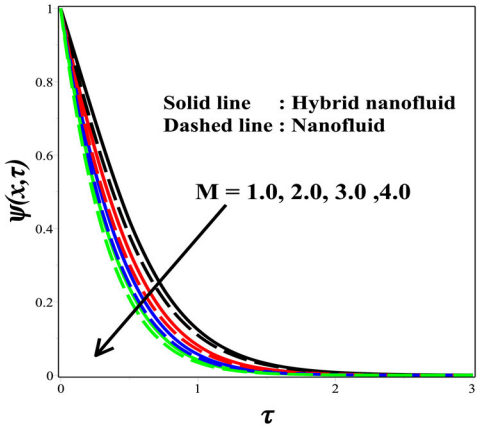

FIGURE 5. Effect of M on $\Psi(x, \tau)$.

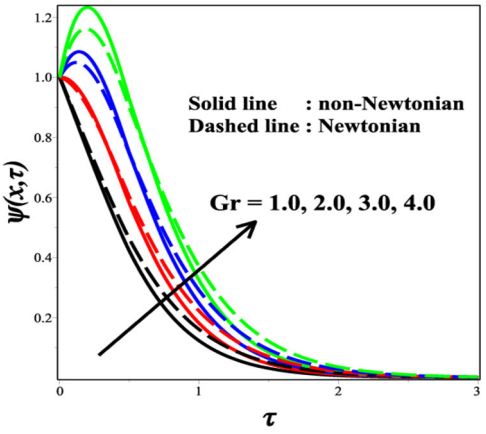

FIGURE 6. Influence of Gr on $\Psi(x, \tau)$.

TABLE 3. Skin friction coefficient results for various physical parameters at $\beta = 0.5$, $\phi_1 = 0.02$, $\phi_2 = 0.02$.

M	Gr	K	τ	C_{fx}	
				Numerical Method	Analytical Method
0.5	5.0	1.0	0.2	-0.572036	-0.572021
1.0	5.0	1.0	0.2	-0.601170	-0.601165
1.5	5.0	1.0	0.2	-0.629742	-0.629723
0.5	6.0	1.0	0.2	-0.463291	-0.463212
0.5	7.0	1.0	0.2	-0.355108	-0.355107
0.5	5.0	1.5	0.2	-0.548127	-0.548155
0.5	5.0	2.0	0.2	-0.536032	-0.536011
0.5	5.0	1.0	0.3	-0.764629	-0.764678
0.5	5.0	1.0	0.4	-0.894940	-0.894921

TABLE 4. Nusselt number results for various physical parameters.

Pr	Nr	Ec	Q	$\emptyset_1$	$\emptyset_2$	τ	$Nu_x Re_x^{-1}$	
							Numerical Method	Analytical Method
16.62	0.5	0.01	0.5	0.01	0.01	0.2	0.621182	0.621182
17.00	0.5	0.01	0.5	0.01	0.01	0.2	0.628245	0.628245
18.00	0.5	0.01	0.5	0.01	0.01	0.2	0.646459	0.646459
16.62	1.0	0.01	0.5	0.01	0.01	0.2	0.715537	0.715537
16.62	1.5	0.01	0.5	0.01	0.01	0.2	0.798822	0.798822
16.62	0.5	0.1	0.5	0.01	0.01	0.2	0.557743	0.557743
16.62	0.5	0.2	0.5	0.01	0.01	0.2	0.369731	0.369731
16.62	0.5	0.01	1.0	0.01	0.01	0.2	1.228217	1.228217
16.62	0.5	0.01	1.5	0.01	0.01	0.2	1.806017	1.806017
16.62	0.5	0.01	0.5	0.02	0.01	0.2	0.630368	0.630368
16.62	0.5	0.01	0.5	0.03	0.01	0.2	0.639722	0.639722
16.62	0.5	0.01	0.5	0.01	0.02	0.2	0.621153	0.621153
16.62	0.5	0.01	0.5	0.01	0.03	0.2	0.621123	0.621123
16.62	0.5	0.01	0.5	0.01	0.01	0.3	0.757743	0.757743
16.62	0.5	0.01	0.5	0.01	0.01	0.4	0.869731	0.869731

B. EFFECT OF Pr, Q, Nr AND Ec ON THE TEMPERATURE PROFILES $\Theta(x, \tau)$

The temperature profiles are visually represented in Figs. (12)-(18), it shows the influence of several parameters like Prandtl number (Pr), thermal radiation parameter (Nr), heat source/sink parameter (Q), and Eckert number (Ec). In Figs. 12 and 13 show the generation/absorption parameter Q in the temperature patterns $\Theta(x, \tau)$ over an infinite vertical flat plate. Fig. 12 displays a comparison between the results obtained from Newtonian and non-Newtonian situations. On the other hand, Fig. 13 compares the performance of nanofluid and hybrid nanofluid. For all scenarios, it is noticed that when the variable Q increases, the temperature variation gets larger. Physically, the thermal field process involves the addition of extra heat to a system, resulting in an increase in the temperature profile. Figs. 14 and 15 illustrate thermal radiation parameters Nr in the temperature profiles

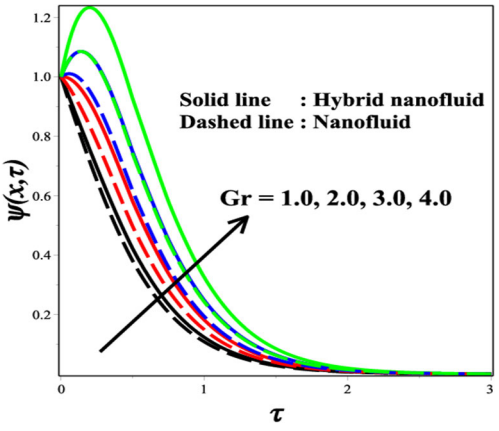

FIGURE 7. Effect of Gr on $\Psi(x, \tau)$.

TABLE 5. Probable error (PE), Correlation coefficient (r) and $|r/PE|$ values of C_{fx} with respect to influence parameters M, Gr, and K.

Parameters	r	PE	$\lvert r/PE \rvert$
M	-0.99998419	1.23117E-05	81222.45366
Gr	1	0	∞
K	1	0	∞
τ	-1	0	∞

$\Theta(x, \tau)$. Fig. 14 presents a comparison between Newtonian and non-Newtonian fluids outcomes, while Fig. 15 compares nanofluid and hybrid nanofluid over an infinite vertical flat plate. Both comparison analysis indicates that raising the heat radiation parameter Nr enhances the temperature profile. Physically, it shows that the average absorption coefficient decreases as the thermal radiation parameter increases. Consequently, the temperature profile has increased. Figs. 16 and 17 show how temperature profile $\Theta(x, \tau)$ variations affect the Eckert number (Ec). Here, Fig. 16 compares Newtonian and non-Newtonian situations. Fig. 17 utilizes the same parameter Ec but presents a distinct comparison between hybrid nanofluid and nanofluid. In both cases, it is observed that as Ec increases, the temperature range gets more intense. The heated fraction appears to generate heat in the fluid, causing Ec to expand into the heated fraction. In a purely physical sense, it converts kinetic energy into internal energy, leading to improved temperatures throughout the fluid's region. Fig. 18 shows the impact of the Prandtl number (Pr) on the temperature profile $\Theta(x, \tau)$ for Newtonian and non-Newtonian situations. In this case, there is an inverse relationship between the temperature and the Prandtl number, meaning that as the Pr increases, the temperature lowers. By increasing the Prandtl number, thermal conductivity decreases, resulting in a reduced heat transfer rate and a subsequent reduction in temperature. Figs. 19 and 20 visualize the velocity profile $\Psi(x, \tau)$ and the temperature profiles $\Theta(x, \tau)$ in three dimensions.

TABLE 6. Probable error (*PE*), Correlation coefficient (*r*) and $|r/PE|$ values of $Nu_x Re_x^{-1}$ with respect to parameters *Pr*, *Nr*, *Ec*, *Q*, ϕ_1 and ϕ_2.

Parameters	*r*	*PE*	*|r/PE|*
Pr	0.999990593	7.32652E-06	136489.2262
Nr	1	0	∞
Ec	-1	0	∞
Q	1	0	∞
ϕ_1	1	0	∞
ϕ_2	1	0	∞
τ	1	0	∞

TABLE 7. Multiple linear regression model for C_{fx}, Number of observations: 9.

Variables	Estimate value	Standard Error	t stat	p-value
Intercept	-0.82799	0.079723	-10.3858	0.000485
M	-0.05109	0.017289	-2.95507	0.041758
Gr	0.041758	0.008644	12.94309	0.000206
K	0.045096	0.017289	2.608398	0.05952
τ	-1.64316	0.086444	-19.0084	4.51E-05

TABLE 8. Multiple linear regression model for $Nu_x Re_x^{-1}$, Number of observations:15.

Variables	Estimate value	Standard error	t stat	p-value
Intercept	-0.36162	0.29994	-1.20566	0.26712
Pr	0.0066	0.0160	0.4164	0.6896
Nr	0.1635	0.0211	7.7461	0.0001
Ec	-1.2963	0.1119	-11.581	8.07E-06
Q	1.1744	0.0211	55.610	1.59E-10
$\emptyset_1$	0.1087	1.0555	0.1030	0.9209
$\emptyset_2$	-0.8196	1.0555	-0.7765	0.4629
τ	1.1857	0.1056	11.233	0.4629

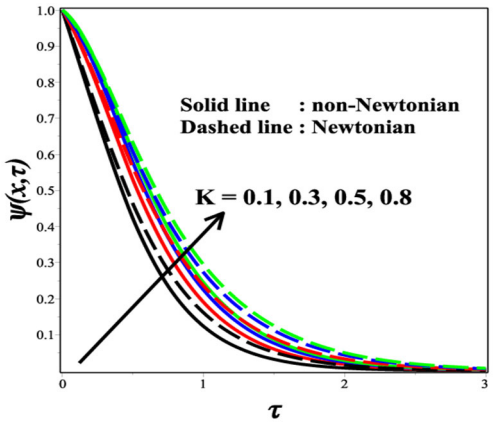

FIGURE 8. Influence of *K* on $\Psi(x, \tau)$.

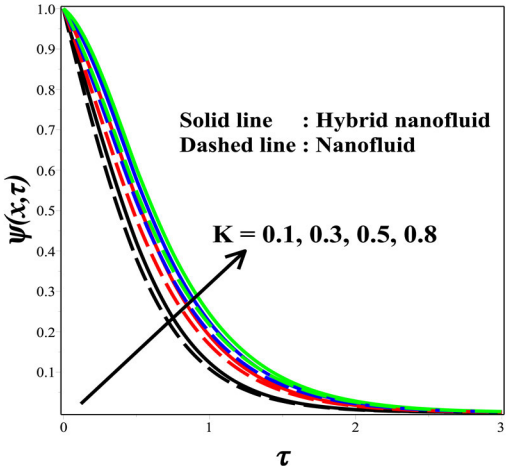

FIGURE 9. Effect of *K* on $\Psi(x, \tau)$.

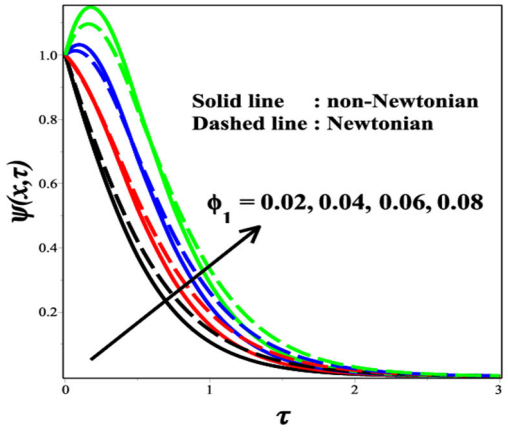

FIGURE 10. Influence of $\emptyset_1$ on $\Psi(x, \tau)$.

C. VARIATION OF SKIN FRICTION COEFFICIENT AND NUSSELT NUMBER

The influence of these parameters on the skin friction coefficient (C_{fx}) and the Nusselt number (Nu_x) are shown in Tables 3 and 4. Table 3 represents the estimated C_{fx} values for different combinations of M, Gr, and K while keeping the amounts of other components constant. The drag coefficient demonstrates a positive correlation with the Grashof number, and permeability parameter while exhibiting a negative correlation with the magnetic parameter. Table 4 presents the estimated Nu_x values for different combinations of *Pr, Nr, Q, Ec*, ϕ_1 and ϕ_2. The Nusselt number has a positive correlation with the thermal radiation parameter, heat source parameter, Prandtl number, volume fraction of nanoparticles ϕ_1. Conversely, it demonstrates a negative correlation with the Eckert number and the volume fraction of nanoparticles ϕ_2.

TABLE 9. Mean absolute deviation, root mean square error, mean squared error, and mean absolute percentage error values with respect to actual (C_{fx}) and predicted values.

PV	AV	
-0.57764	-0.57204	
-0.60319	-0.60117	
-0.62873	-0.62974	MAD = 0.0063
-0.46576	-0.46329	MSE = 8.30E-05
-0.35387	-0.35511	RMSE = 0.0091
-0.5551	-0.54813	MAPE = 94.5%
-0.53255	-0.53603	
-0.74196	-0.76463	
-0.90627	-0.89494	

TABLE 10. Mean absolute deviation, mean squared error, root mean square error and mean absolute percentage error values with respect to actual ($Nu_x Re_x^{-1}$) and predicted values.

PV	AV	
0.634793	0.62118	
0.637317	0.62825	
0.643961	0.64646	MAD =0.0078
0.716553	0.71554	MSE =1.56E-04
0.798314	0.79882	RMSE =0.0125
0.518126	0.55774	MAPE =136.91%
0.388497	0.36973	
1.221967	1.22822	
1.809142	1.80602	
0.635879	0.63037	
0.636966	0.63972	
0.626597	0.62115	
0.618401	0.62112	
0.753358	0.75774	
0.871923	0.86973	

VII. METHOD OF STATISTICAL ANALYSIS

Statistical methods for exploring numerical and estimated results such as multiple linear regression, probable error (PE), and correlation coefficient (r) have been attracting a lot of attention in the scientific community. The present study employs statistical analysis of relevant parameters to examine the relationship between physical quantities like Nusselt number and the skin friction coefficient.

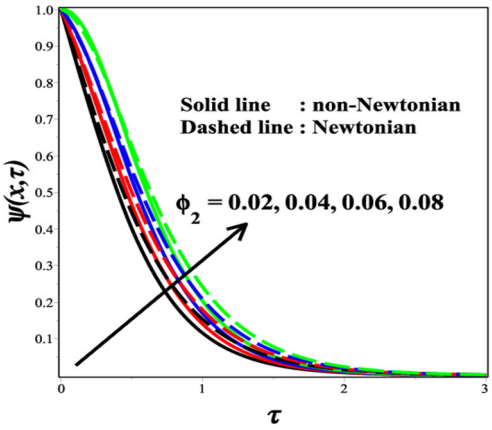

FIGURE 11. Influence of $\emptyset_2$ on $\Psi(x, \tau)$.

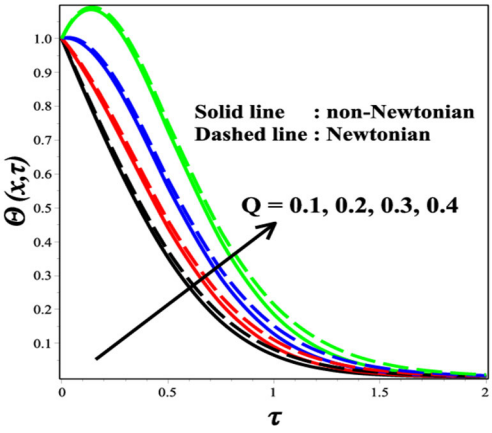

FIGURE 12. Influence of Q on $\Theta(x, \tau)$.

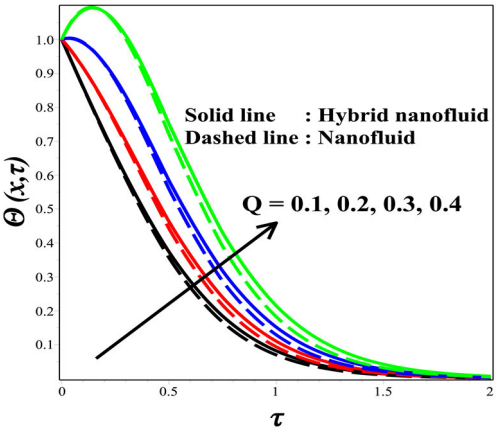

FIGURE 13. Effect of Q on $\Theta(x, \tau)$.

A. CORRELATION COEFFICIENT AND PROBABLE ERROR

The correlation coefficient is a statistical measure of the degree of connection between two or more independent variables. The magnitude of an association is represented by the correlation coefficient (r), where $r \in [-1, 1]$ and the

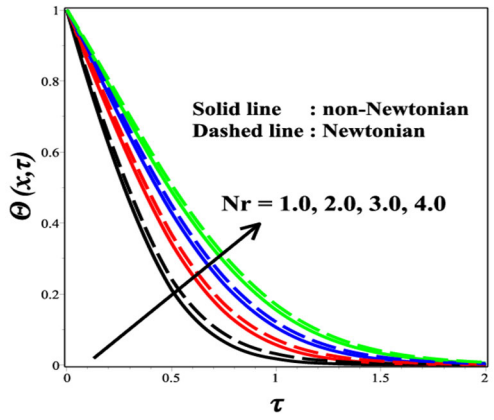

FIGURE 14. Influence of *Nr* on $\Theta(x, \tau)$.

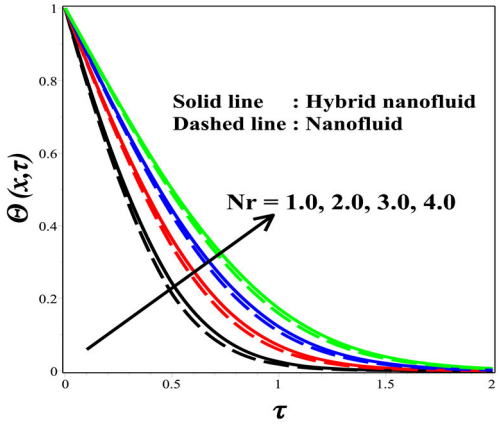

FIGURE 15. Effect of *Nr* on $\Theta(x, \tau)$.

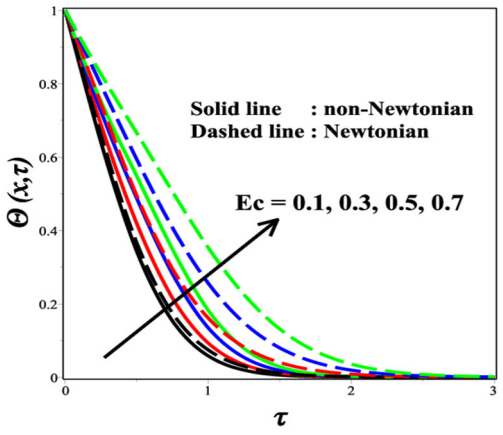

FIGURE 16. Influence of *Ec* on $\Theta(x, \tau)$.

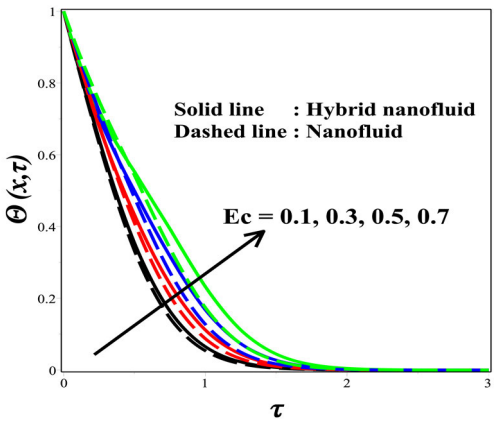

FIGURE 17. Effect of *Ec* on $\Theta(x, \tau)$.

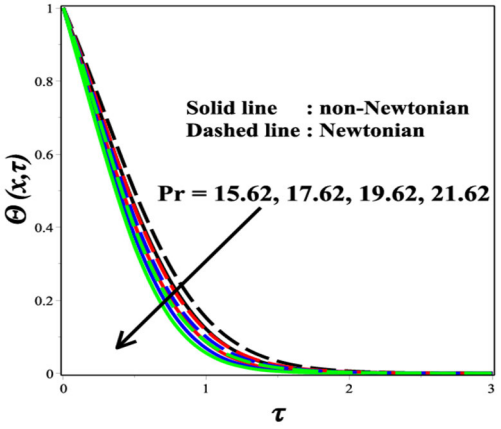

FIGURE 18. Influence of *Pr* on $\Theta(x, \tau)$.

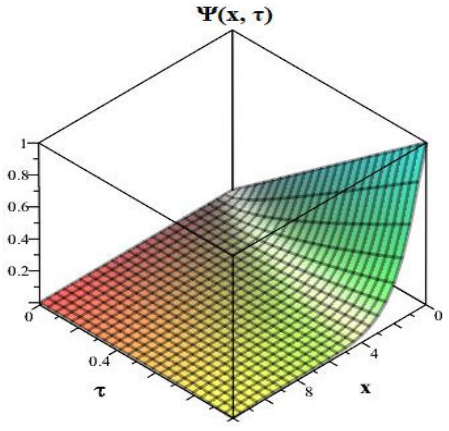

FIGURE 19. 3D view on velocity profile.

relationship direction is indicated by the symbol r. The reliability coefficient denoted as r, can be assessed by calculating the probable error (PE). The study applies the formula $\mathrm{PE} = \left(\frac{1-r^2}{\sqrt{n}}\right)0.6745$, where n represents the total number of data. If the value of the correlation coefficient $\left|\frac{r}{PE}\right|>6$, it has been considered to be statistically significant. Based on the data presented in Table 5, it can be determined C_{fx} is negatively correlation with the Magnetic parameter (M) and positively correlation with the Grashof number (Gr) and permeability parameter (K). Table 6 shows that $Nu_x Re_x^{-1}$ exhibits a positive correlation with Prandtl number (Pr), heat source parameter (Q), thermal radiation parameter (Nr), and volume fraction of nanoparticles (ϕ_1) and negatively correlated with volume fraction (ϕ_2) and Eckert number (Ec).

B. MULTIPLE LINEAR REGRESSION MODELING

Multiple regression modeling is a statistical analytical approach used to determine the relationship between one dependent variable and many independent variables. The

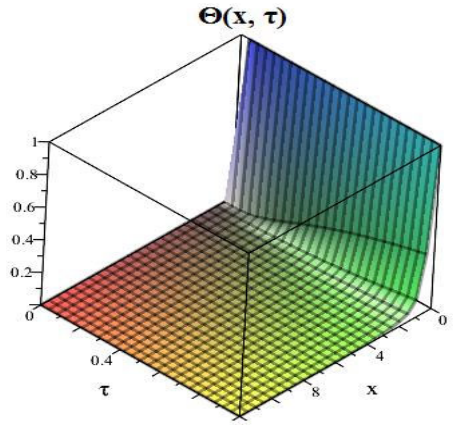

FIGURE 20. 3D view on temperature profile.

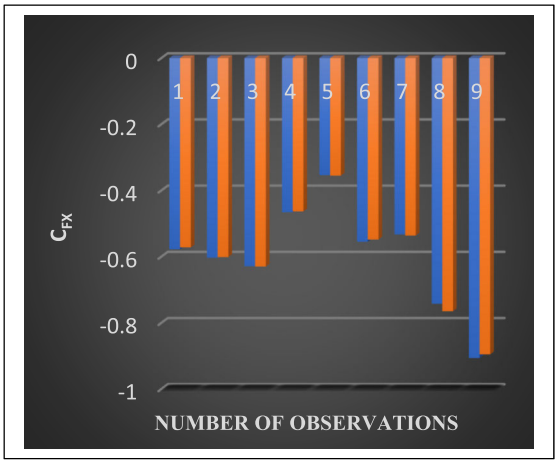

FIGURE 21. Estimated and actual values for C_{f_x}.

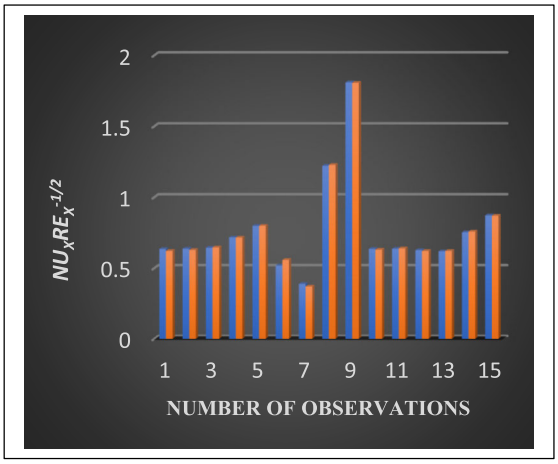

FIGURE 22. Estimated and actual values for $Nu_x Re_x^{-1/2}$.

multiple linear regression method is used to estimate (C_{fx}) and ($Nu_x Re_x^{-1}$)because all pertinent correlations have been verified. Some generalized definitions of the calculated examples are as follows:

$$\begin{aligned} C_{f_{est}} &= a + b_M M + b_{Gr} Gr + b_K K + b_\tau \tau \\ \mathrm{Nu}_{est} &= a + b_{\mathrm{Pr}} \mathrm{Pr} + b_{Nr} Nr + b_{Ec} Ec + b_Q Q \\ &\quad + b_{\phi_1} \phi_1 + b_{\phi_2} \phi_2 + b_\tau \tau \end{aligned}$$

where $a, b_M, b_{Gr}, b_K, b_{pr}, b_{Nr}, b_{Ec}, b_Q, b_{\phi_1}, b_{\phi_2}, b_\tau$ are estim-ated regression coefficients. In tables 7 and 8 represents the multiple linear regression model for physical quantities. The estimated regression values for C_f and Nu are:

$$\begin{aligned} C_{f_{est}} &= -0.82799 - 0.05109\, M + 0.041758 Gr \\ &\quad + 0.045096\, K - 1.64316\tau \\ \mathrm{Nu}_{est} &= -0.36162 + 0.00664 Pr + 0.16352 Nr \\ &\quad - 1.29629 Ec + 1.17435\, Q + 0.10869\phi_1 \\ &\quad - 0.81957\phi_2 + 1.18565\tau \end{aligned}$$

An estimated value for the regression coefficient with a positive value indicates an increase in skin friction coefficient or Nusselt number, while a negative value indicates a decrease in skin friction coefficient or Nusselt number. The estimated models show that the skin friction coefficient decreases with larger values M and increases with Gr and k. Additionally, the Nusselt number increases with Pr, Nr, Q and ϕ_1 then decreases with higher values of Ec and ϕ_2.Those outcomes completely correspond with the details shown in tables 3, 4, 5, 6, 7, and 8. Tables 9 and 10 represents actual values and predicted values and calculate the Mean Squared Error (MSE), Mean Absolute Percentage Error (MAPE), Mean Absolute Deviation (MAD), and Root Mean Squared Error (RMSE). Figs. 21 and 22 are used to evaluate the precision of the developed regression technique within the chosen sample. There is a good correlation between the actual and predicted values for physical quantities.

VIII. CONCLUDING REMARKS

This study explores the influence of a heat source on the behavior of an MHD Casson hybrid nanofluid flowing over an infinite vertical flat plate. The governing partial differential equations have been subjected to a similarity transformation, resulting in a system of partial differential equations. The numerical approach used to solve these equations is the implicit finite difference method, namely the Crank-Nicolson scheme. Furthermore, the perturbation method is utilized for analytical computations. An analysis is conducted to compare numerical and analytical results. As a result, comparisons between analytical and numerical results are more accurate. The outcomes are presented in tabular and graphical representations to illustrate the influence of effective parameters. Further, multiple linear regression has been employed to statistically evaluate the impact of relevant parameters on the physical quantities. The most significant quantitative findings of the current investigation can be characterized as follows

- When the magnetic parameter (M) is increased, the velocity decreases whereas if the Grashof number (Gr) is increased, the velocity increases for Newtonian and non-Newtonian scenarios as well as hybrid nanofluid and nanofluid situations.
- In both Newtonian and non-Newtonian situations, as well as in scenarios involving nanofluids and hybrid nanofluids, a rise in the heat source parameter (Q) leads

to an increase in temperature. However, an increase in the Prandtl number (Pr) results in a decrease in temperature.

- The rate of heat transfer (Nusselt number) has a positive correlation with the thermal radiation parameter, Prandtl number, heat source parameter, and volume fraction of nanoparticles while showing a negative correlation with the Eckert number.
- The drag coefficient (skin friction coefficient) exhibits a positive correlation with the permeability parameter while exhibiting a negative correlation with the magnetic parameter.
- For the skin friction coefficient, the estimation of the regression model is given by

$$C_{f_{est}} = -0.82799 - 0.05109\,M + 0.041758Gr + 0.045096\,K - 1.64316$$

- For the Nusselt number, the estimation of the regression model is given by

$$\mathrm{N}u_{est} = -0.36162 + 0.00664Pr + 0.16352Nr - 1.29629Ec + 1.17435\,Q + 0.10869\phi_1 - 0.81957\phi_2 + 1.18565\tau$$

NOMENCLATURE

B_0	Magnetic strength [Wbm^{-1}]
A	Acceleration
g	gravity force ($\mathrm{m/s}^2$)
Gr	Grashoff number
Nr	Thermal Radiation parameter
M	Magnetic parameter
K	Permeability parameter
Pr	Prandtl number
Q	heat source/sink Parameter
Q_0	dimensional heat source
Ec	Eckert number
Re_x	Reynolds number
$\mathrm{H_2O}$	water
t	Dimensional time [s]
T	Dimensional temperature [K]
T_∞	Ambient temperature [K]
T_w	Surface temperature [K]
x, y	Cartesian co-ordinates [m]
Nu_x	Nusselt number
C_{fx}	Skin friction coefficients

GREEK SYMBOLS

β	Casson fluid parameter
β_r	Mean absorption coefficient
ρ	Density [Kgm^{-3}]
Θ	Dimensionless temperature
τ	Dimensionless time
ϑ_f	Kinematic viscosity [$\mathrm{m}^{-2}\mathrm{s}^{-1}$]
κ	Thermal conductivity [$\mathrm{Wm}^{-1}\mathrm{K}^{-1}$]
μ	Dynamic viscosity [$\mathrm{N\,s\,m}^{-2}$]
σ_e	Stefan–Boltzmann constant [$\mathrm{Wm}^{-2}\,\mathrm{K}^{-4}$]
Ψ^* , ν^*	Dimensional velocity components [ms^{-1}]
Ψ , ν	Dimensionless velocity
ϕ_1	Volume fraction of nanoparticles (CuO)
ϕ_2	Volume fraction of nanoparticles (MgO)

SUBSCRIPTS

∞	Infinity
f	Base Fluid
nf	nanofluid
hnf	hybrid nanofluid

REFERENCES

[1] R. P. Chhabra, "Non-Newtonian fluids: An introduction," in *Rheology of Complex Fluids*. Boca Raton, FL, USA: CRC Press, 2010, pp. 1–33.
[2] S. C. Hauswirth, C. A. Bowers, C. P. Fowler, P. B. Schultz, A. D. Hauswirth, T. Weigand, and C. T. Miller, "Modeling cross model non-newtonian fluid flow in porous media," *J. Contaminant Hydrol.*, vol. 235, Nov. 2020, Art. no. 103708, doi: 10.1016/j.jconhyd.2020.103708.
[3] N. Ali, M. Sajid, Z. Abbas, and T. Javed, "Non-newtonian fluid flow induced by peristaltic waves in a curved channel," *Eur. J. Mech. B/Fluids*, vol. 29, no. 5, pp. 387–394, Sep. 2010, doi: 10.1016/j.euromechflu.2010.04.002.
[4] M. Saqib, F. Ali, I. Khan, and N. A. Sheikh, "Heat and mass transfer phenomena in the flow of Casson fluid over an infinite oscillating plate in the presence of first-order chemical reaction and slip effect," *Neural Comput. Appl.*, vol. 30, no. 7, pp. 2159–2172, Oct. 2018, doi: 10.1007/s00521-016-2810-x.
[5] P. B. Anki Reddy, "MHD boundary layer slip flow of a Casson fluid over an exponentially stretching surface in the presence of thermal radiation and chemical reaction," *J. Nav. Archit. Mar. Eng.*, vol. 13, no. 2, pp. 165–177, Dec. 2016, doi: 10.3329/jname.v13i2.23537.
[6] D. Das, S. Shaw, K. K. Mondal, and R. R. Kairi, "Analyzing the impact of boundary slip and absorption effects on the dispersion of solute in a pulsatile channel flow of Casson fluid under magnetic field," *Eur. Phys. J. Plus*, vol. 138, no. 5, pp. 1–20, May 2023, doi: 10.1140/epjp/s13360-023-03973-8.
[7] K. Bhattacharyya, M. S. Uddin, and G. C. Layek, "Exact solution for thermal boundary layer in Casson fluid flow over permeable shrinking sheet with variable wall temperature and thermal radiation," *Alexandria Eng. J.*, vol. 55, no. 2, pp. 1703–1712, Jun. 2016, doi: 10.1016/j.aej.2016.03.010.
[8] S. U. S. Choi, "Enhancing thermal conductivity of fluids with nanoparticles," in *Proc. Amer. Soc. Mech. Eng., Fluids Eng. Division FED*, vol. 231, 1995, pp. 99–105.
[9] T. Hayat, K. Muhammad, T. Muhammad, and A. Alsaedi, "Melting heat in radiative flow of carbon nanotubes with homogeneous-heterogeneous reactions," *Commun. Theor. Phys.*, vol. 69, no. 4, p. 441, Apr. 2018, doi: 10.1088/0253-6102/69/4/441.
[10] M. Gupta, V. Singh, R. Kumar, and Z. Said, "A review on thermophysical properties of nanofluids and heat transfer applications," *Renew. Sustain. Energy Rev.*, vol. 74, pp. 638–670, Jul. 2017, doi: 10.1016/j.rser.2017.02.073.
[11] R. K. Tiwari and M. K. Das, "Heat transfer augmentation in a two-sided lid-driven differentially heated square cavity utilizing nanofluids," *Int. J. Heat Mass Transf.*, vol. 50, nos. 9–10, pp. 2002–2018, May 2007, doi: 10.1016/j.ijheatmasstransfer.2006.09.034.
[12] M. Tayyab, I. Siddique, F. Jarad, M. K. Ashraf, and B. Ali, "Numerical solution of 3D rotating nanofluid flow subject to darcy-forchheimer law, bio-convection and activation energy," *South Afr. J. Chem. Eng.*, vol. 40, pp. 48–56, Apr. 2022, doi: 10.1016/j.sajce.2022.01.005.
[13] R. S. R. Gorla and M. Kumari, "Mixed convective boundary layer flow over a vertical wedge embedded in a porous medium saturated with a nanofluid: Entire regime," *Proc. Inst. Mech. Engineers, N, J. Nanoengineering Nanosystems*, vol. 225, no. 2, pp. 55–66, Jun. 2011, doi: 10.1177/1740349911434248.
[14] M. Yasir, M. Khan, A. S. Alqahtani, and M. Y. Malik, "Mass transpiration effect on rotating flow of radiative hybrid nanofluid due to shrinking surface with irregular heat source/sink," *Case Stud. Thermal Eng.*, vol. 44, Apr. 2023, Art. no. 102870, doi: 10.1016/j.csite.2023.102870.

[15] M. Kursus, P. J. Liew, N. A. Che Sidik, and J. Wang, "Recent progress on the application of nanofluids and hybrid nanofluids in machining: A comprehensive review," *Int. J. Adv. Manuf. Technol.*, vol. 121, nos. 3–4, pp. 1455–1481, Jul. 2022, doi: 10.1007/s00170-022-09409-4.

[16] N. Akkurt, T. Shedd, A. A. Memon, Usman, M. R. Ali, and M. Bouye, "Analysis of the forced convection via the turbulence transport of the hybrid mixture in three-dimensional L-shaped channel," *Case Stud. Thermal Eng.*, vol. 41, Jan. 2023, Art. no. 102558, doi: 10.1016/j.csite.2022.102558.

[17] J. Shaik, B. A. R. Polu, M. Mohamed Ahmed, and R. Ahmed Mohamed, "Characteristics of moving hot block and non-Fourier heat flux model on sinusoidal wavy cavity filled with hybrid nanofluid," *Eur. Phys. J. Plus*, vol. 137, no. 1, pp. 1–16, Jan. 2022, doi: 10.1140/epjp/s13360-022-02361-y.

[18] V. Rajesh, M. A. Sheremet, and H. F. Öztop, "Impact of hybrid nanofluids on MHD flow and heat transfer near a vertical plate with ramped wall temperature," *Case Stud. Thermal Eng.*, vol. 28, Dec. 2021, Art. no. 101557, doi: 10.1016/j.csite.2021.101557.

[19] B. Ahmed, T. Hayat, F. M. Abbasi, and A. Alsaedi, "Mixed convection and thermal radiation effect on MHD peristaltic motion of powell-eyring nanofluid," *Int. Commun. Heat Mass Transf.*, vol. 126, Jul. 2021, Art. no. 105320, doi: 10.1016/j.icheatmasstransfer.2021.105320.

[20] U. S. Mahabaleshwar, K. R. Nagaraju, P. N. V. Kumar, M. N. Nadagoud, R. Bennacer, and D. Baleanu, "An MHD viscous liquid stagnation point flow and heat transfer with thermal radiation and transpiration," *Thermal Sci. Eng. Prog.*, vol. 16, May 2020, Art. no. 100379, doi: 10.1016/j.tsep.2019.100379.

[21] S. R. R. Reddy and P. B. A. Reddy, "Numerical simulations of unsteady 3D MHD micropolar fluid flow over a slendering sheet," *J. Appl. Comput. Mech.*, vol. 7, no. 3, pp. 1403–1412, 2021, doi: 10.22055/jacm.2020.31062.1821.

[22] Y. D. Reddy and B. Shankar Goud, "Comprehensive analysis of thermal radiation impact on an unsteady MHD nanofluid flow across an infinite vertical flat plate with ramped temperature with heat consumption," *Results Eng.*, vol. 17, Mar. 2023, Art. no. 100796, doi: 10.1016/j.rineng.2022.100796.

[23] M. Vijatha and P. B. A. Reddy, "Comparative analysis on magnetohydrodynamic flow of non-newtonian hybrid nanofluid over a stretching cylinder: Entropy generation," *Proc. Inst. Mech. Engineers, E, J. Process Mech. Eng.*, vol. 236, no. 6, pp. 2361–2371, Dec. 2022, doi: 10.1177/09544089221093296.

[24] P. B. Anki Reddy, S. Jakeer, H. T. Basha, S. R. Reddisekhar Reddy, and T. M. Kumar, "Multi-layer artificial neural network modeling of entropy generation on MHD stagnation point flow of cross-nanofluid," *Waves Random Complex Media*, vol. 138, pp. 1–28, Apr. 2022, doi: 10.1080/17455030.2022.2067375.

[25] A. H. Ganie, Zeeshan, A. M. Mahnashi, A. Shafee, R. Shah, and D. Fathima, "Comparative analysis of Casson nanofluid flow over shrinking sheet under the influence of thermal radiation, electric variable, and cross diffusions: Multiple solutions and stability analysis," *IEEE Access*, p. 1, 2024, doi: 10.1109/ACCESS.2024.3404118.

[26] I. Chabani, F. Mebarek-Oudina, and A. A. I. Ismail, "MHD flow of a hybrid nano-fluid in a triangular enclosure with zigzags and an elliptic obstacle," *Micromachines*, vol. 13, no. 2, p. 224, Jan. 2022.

[27] A. J. Chamkha, "Hydromagnetic three-dimensional free convection on a vertical stretching surface with heat generation or absorption," *Int. J. Heat Fluid Flow*, vol. 20, no. 1, pp. 84–92, Feb. 1999.

[28] M. Khan and A. Hamid, "Influence of non-linear thermal radiation on 2D unsteady flow of a Williamson fluid with heat source/sink," *Results Phys.*, vol. 7, pp. 3968–3975, Jun. 2017, doi: 10.1016/j.rinp.2017.10.014.

[29] S. R. R. Reddy and P. B. A. Reddy, "Impact of thermal radiation and viscous dissipation on hydromagnetic unsteady flow over an exponentially inclined preamble stretching sheet," *J. Comput. Appl. Res. Mech. Eng.*, vol. 10, no. 1, pp. 171–181, 2020, doi: 10.22061/jcarme.2019.3709.1433.

[30] N. A. M. Alkuhayli, "Heat transfer analysis of a hybrid nanofluid flow on a rotating disk considering thermal radiation effects," *Case Stud. Thermal Eng.*, vol. 49, Sep. 2023, Art. no. 103131, doi: 10.1016/j.csite.2023.103131.

[31] M. A. Kumar, Y. D. Reddy, V. S. Rao, and B. S. Goud, "Thermal radiation impact on MHD heat transfer natural convective nano fluid flow over an impulsively started vertical plate," *Case Stud. Thermal Eng.*, vol. 24, Apr. 2021, Art. no. 100826, doi: 10.1016/j.csite.2020.100826.

[32] A. Jaafar, I. Waini, A. Jamaludin, R. Nazar, and I. Pop, "MHD flow and heat transfer of a hybrid nanofluid past a nonlinear surface stretching/shrinking with effects of thermal radiation and suction," *Chin. J. Phys.*, vol. 79, pp. 13–27, Oct. 2022, doi: 10.1016/j.cjph.2022.06.026.

[33] P. Jalili, A. A. Azar, B. Jalili, and D. D. Ganji, "Study of nonlinear radiative heat transfer with magnetic field for non-newtonian Casson fluid flow in a porous medium," *Results Phys.*, vol. 48, May 2023, Art. no. 106371, doi: 10.1016/j.rinp.2023.106371.

[34] B. S. Goud, Y. D. Reddy, S. R. Mishra, M. I. Khan, K. Guedri, and A. M. Galal, "Thermal radiation impact on magneto-hydrodynamic heat transfer micropolar fluid flow over a vertical moving porous plate: A finite difference approach," *J. Indian Chem. Soc.*, vol. 99, no. 8, Aug. 2022, Art. no. 100618, doi: 10.1016/j.jics.2022.100618.

[35] B. P. Reddy, A. Felician, and P. M. Matao, "Finite element simulation of soret-dufour and conjugate heating effects on mixed convective heat absorbing hydromagnetic Casson fluid flow with suction/blowing from flat semi-infinite vertical porous plate," *Heliyon*, vol. 10, no. 2, Jan. 2024, Art. no. e24150, doi: 10.1016/j.heliyon.2024.e24150.

[36] V. Rajesh and A. J. Chamkha, "Impact of hybrid nanofluids on unsteady MHD flow and heat transfer due to a moving infinite vertical plate," *Heat Transf.*, vol. 51, no. 2, pp. 1358–1375, Mar. 2022, doi: 10.1002/htj.22355.

[37] O. Mahitha, V. K. A. Golla, H. F. Öztop, and N. H. Abu-Hamedeh, "Investigation of MHD natural convective flow of optically thick medium-radiating CNT Casson nanofluid over an infinite flat plate with reference to caputo fractional derivative: As an application to water purification," *J. Magn. Magn. Mater.*, vol. 567, Feb. 2023, Art. no. 170330, doi: 10.1016/j.jmmm.2022.170330.

[38] K. Sakkaravarthi and P. B. A. Reddy, "Entropy optimization of MHD hybrid nanofluid flow through a curved stretching sheet with thermal radiation and heat generation: Semi-analytical and numerical simulations," *Proc. Inst. Mech. Engineers, E, J. Process Mech. Eng.*, vol. 237, no. 2, pp. 138–148, Apr. 2023, doi: 10.1177/09544089221100222.

[39] M. Shuaib, A. Ali, M. A. Khan, and A. Ali, "Numerical investigation of an unsteady nanofluid flow with magnetic and suction effects to the moving upper plate," *Adv. Mech. Eng.*, vol. 12, no. 2, Feb. 2020, Art. no. 168781402090358, doi: 10.1177/1687814020903588.

KEERTHIGA M received the B.Sc. degree in mathematics from the D.K.M. College for Women, in 2019, and the M.Sc. degree in mathematics from Muthuragam Government Arts College, in 2021. She is currently pursuing the Ph.D. degree in applied mathematics with the Department of Mathematics, Vellore Institute of Technology, Vellore, Tamil Nadu, India. She is doing her research work under the guidance of Dr. P. Bala Anki Reddy. Her research interests include heat transfer, fluid dynamics, MHD flows, nanofluids, hybrid nanofluids, analytical, and numerical solutions.

P. BALA ANKI REDDY was born in Andhra Pradesh, India. He received the M.Sc. and Ph.D. degrees in mathematics from Sri Venkateshwara University, Tirupati, Andhra Pradesh. Currently, he is working as an Associate Professor with the Department of Mathematics, VIT University, Vellore, Tamil Nadu. He has published several articles in national and international journals. His research interests include application of flow separation, particularly bio-fluid dynamics and the analysis of boundary layer flows in Newtonian and non-Newtonian fluids, including heat and mass transfer in porous and non-porous media. His current research interest includes nanofluid flow problems with entropy generations. He attended several workshops, seminars, and faculty development programs. Also, he was recognized as the Top 2% Scientist in the World by Stanford University, USA, and Elsevier BV for the years 2022 and 2023 (single year). Moreover, he received the Top1% Citation Award from IOP Publication, in 2023.